General purpose potential for glassy and crystalline phases of Cu-Zr alloys based on the ACE formalism

Niklas Leimeroth, Jochen Rohrer, and Karsten Albe
Institut für Materialwissenschaft, Technische Universität Darmstadt, Otto-Berndt-Str. 3, 64287 Darmstadt, Germany

(Received 1 November 2023; accepted 13 February 2024; published 16 April 2024)

A general purpose machine-learning interatomic potential (MLIP) for the Cu-Zr system is presented based on the atomic cluster expansion formalism [R. Drautz, Phys. Rev. B **99**, 014104 (2019)]. By using an extensive set of Cu-Zr training data generated withdensity functional theory, this potential describes a wide range of properties of crystalline as well as amorphous phases within the whole compositional range. Therefore, the machine learning interatomic potential (MLIP) can reproduce the experimental phase diagram and amorphous structure with considerably improved accuracy. A massively different short-range order compared to classica interatomic potentials is found in glassy Cu-Zr samples, shedding light on the role of the full icosahedral motif in the material. Tensile tests of B2-CuZr inclusions in an $Cu_{50}Zr_{50}$ amorphous matrix reveal the occurrence of martensitic phase transformations in this crystal-glass nanocomposite.

DOI: 10.1103/PhysRevMaterials.8.043602

I. INTRODUCTION

Cu-Zr based alloys are among the most studied systems in atomistic simulations of metallic glassess (MGss) [1–6]. Cu-Zr exhibits a complex phase diagram with various intermetallic phases [7–12] and is known to form an amorphous phase in a wide compositional range [13–16].

MGss often show high strength, large elastic strain limits, and hardness, as well as better corrosion and wear resistance compared to crystalline phases of the same materials [17–19], but do not exhibit work hardening and tend to fail catastrophically under high loads due to shear band localization. Embedding nanocrystallites into an amorphous matrix can improve their ductility [20–22]. The deformation mechanisms in such systems, however, are complex and difficult to investigate, experimentally.

Classical molecular dynamics (MD) simulations that rely on empirical interatomic potentials (IPs) continue to play in an important role in understanding the structural, thermodynamical, and mechanical properties of MGss [4,23–26].

Several classical IPs have been developed for Cu-Zr [1,27–32]. Most of them are based on the embedded atom method (EAM) [33], the Finnis-Sinclair, or effective medium theory (EMT) formalisms [34,35], while some also apply the modified embedded atom method (MEAM) [36,37], which extends the EAM with angular-dependent terms. Classical IPs can typically describe selected areas of the Cu-Zr phase space with good accuracy, but do not cover the complex energy landscape and interactions between crystalline and amorphous phases over a wide compositional range.

At this point, machine learning interatomic potentials (MLIPs) offer the possibility of improvements [38,39]. They have seen significant scientific and technical progress over the last two decades and are able to describe different classes of materials with an accuracy close to density functional theory (DFT), while being orders of magnitude faster. Successful developments in the area of atomic environment descriptors include the smooth overlap of atomic positions (SOAP) [40], moment tensor potential [41], and atomic cluster expansion (ACE) [42].

On the technical side, several types of MLIPs have been included in the atomistic simulation code LAMMPS [43] over the last few years, increasing their accessibility and applicability in large-scale simulations.

In the following, we present an Atomic Cluster Expansion (ACE) potential applicable to amorphous and crystalline Cu-Zr over the whole compositional range. By thermodynamic integration, we show that the whole concentration-temperature phase diagram of this binary alloy can be reproduced. Characteristic features of the boundary phases, including stacking fault and defect formation energies, can be described. In combination with MD simulations, we show that the potential can be used to produce glasses with a more accurate local topology than previous potentials and that a B2-CuZr inclusion in an amorphous matrix under load undergoes a martensitic phase transition to the B19' phase in accordance with experiments. Thus, the model opens avenues for studying thermomechanical properties of the binary alloy Cu-Zr with near DFT-accuracy.

II. METHODS

In this paper, the ACE formalism was chosen for fitting a MLIP for the binary alloy Cu-Zr. With GPU acceleration, this potential type outperforms alternative schemes in computational performance at comparable accuracy [44,45]. Hence, in

the context of glassy phases, this Cu-Zr ACE potential eventually allows us to use quench rates of 1×10^{10} K/s for models with a few hundreds or thousands of atoms and 1×10^{11} K/s for hundreds of thousands of atoms, similar to those typically used with EAM potentials.

A. Training data

The choice of training data sets implicitly determines which type of problems can be studied by an interatomic potential and also sets the limit for the achievable accuracy. Since we are aiming for a general purpose potential, the training data set contains a diverse set of structural and chemical information obtained from elemental phases, various intermetallic phases, and amorphous structures in equilibrium and nonequilibrium configurations. For pure Cu and Zr, various lattices (FCC, HCP, BCC, SC, and diamond type) were used. In the case of mixed crystalline phases, the training structures included simple binary phases constructed using the ASE package and all intermetallic Cu-Zr phases from the Materials Project (MP). Amorphous training structures were generated by running cook and quench simulations with the Mendelev Cu-Zr potential from 2009 [30]. Pure crystalline, intermetallic, and amorphous structures were relaxed using DFT. Subsequently, structures with isotropically increased and decreased volume, deformations for elastic constants, grain boundaries, vacancies, interstitials, and surfaces, as well as random atom displacements and cell distortions were created, and their energies and forces were calculated using DFT. Relaxed and modified structures were included in the fit to cover a wide configurational space. The whole compositional range of glasses was covered by using 128 atom structures for the amorphous samples with a Zr content ranging from 20% to 80% in one-atom steps. In total, the training data set amounts to 24 232 structures or 2 168 544 atoms. An additional data set containing 4242 structures with an average size of roughly 118 atoms was used for testing. It contains randomly rattled and deformed structures as well as interfaces between pure Cu and Zr with amorphous structures, where the composition of the amorphous phase was varied from 0% to 100% Zr.

Both data sets were filtered to not contain structures with a maximum absolute force greater than 50 eV/Å, formation enthalpies of 10 eV/atom above the convex hull, a volume per atom of more than 150 Å^3, and a minimal distance between atoms smaller than 1.4 Å.

To probe the robustness of the training data set, we employed the active learning capabilities of the MLIP package [46]. We fitted an additional moment tensor potential and ran cook and quench MD simulations with temperatures up to 3000 K on roughly 500 FCC structures with 108 Cu and Zr atoms randomly assigned to lattice sites. No structures with a high extrapolation grade were found, showing that the training data covers a wide range of configurations up to and including the liquid regime.

DFT calculations were carried out using VASP [47–49] with the Perdew-Burke-Ernzerhof (PBE) exchange-correlation functional [50] and projector augmented wave pseudopotentials [51]. A plane wave energy cutoff of 350 eV and k-point spacings of 0.1 2π Å^{-1} for crystalline phases and 2/13 2π Å^{-1} for amorphous phases were used. The complete set of training data is freely accessible on ZENODO [52].

B. Fitting

We fitted four distinct parametrizations with 514, 1352, 2838, and 6084 basis functions and a cutoff of 7.6 Å. The cutoff corresponds to the value used in several Cu-Zr Embedded Atom Method (EAM) potentials by Mendelev *et al.* [1,30,31]. As expected, more basis functions lead to a higher accuracy for the training data set, but are slower to evaluate. Additionally, the description of the test data set was worse with more functions, indicating overfitting. With the use case of amorphous phases and crystal/glass matrices in mind, we highly valued the increased speed and transferability and decided to use the potential with 514 basis functions. Energies and forces were weighted using energy-based weighting as described in Ref. [53] with Δ_E 0.4 eV and Δ_F 1 eV/Å. Here the weight w_S for a structure is assigned according to the distance of its energy E from the convex hull of formation energies E_h according to

$$w_S = \frac{1}{(E - E_h + \Delta_E)^2} \tag{1}$$

and forces are weighted based on their absolute value F as

$$w_F = \frac{w_S}{F^2 + \Delta_F}. \tag{2}$$

This leads to a higher weight for structures close to the convex hull and for small forces. The relative weight of energies was set to 0.99, that of forces to 0.01. DFT energies were shifted to reproduce the cohesive energies of pure FCC Cu and HCP Zr from the NIST-JANAF thermochemical tables [54].

C. Molecular dynamics simulations

MD simulations were carried out using LAMMPS [43]. Nosé-Hoover thermo- and barostats and a time-step length of 2 fs were applied in all simulations. If not otherwise noted, glass samples were produced by melt quenching from 1700 K to 300 K with a quench rate of 1×10^{11} K/s.

All DFT and MD simulations were performed with the aid of the PYIRON package [55], ensuring a high level of reproducibility. It offers interfaces to several atomistic simulation codes and protocols to calculate properties such as bulk moduli and elastic constants, which were used in this paper.

For moving boundary (MB) calculations, a crystalline structure was equilibrated at the target temperature and a liquid scaled to the same axis lengths in the interface plane was created, only allowing cell changes along the axis normal to the interface. Following this, the crystalline and liquid structures were stacked along the z axis and MD simulations at the target temperature were carried out, again with fixed x and y axis, while the z axis was subject to a barostat. Monitoring the potential energy during the simulation shows which phase grows and therefore whether the target temperature is above or below the melting point.

Bulk moduli were calculated using the corresponding Pyiron protocol. It applies isotropic volume deformation, so the reported values for noncubic cells have a small error due to the neglected anisotropy. Elastic constants were calculated

using Pymatgen [56]. When using DFT, the k mesh was kept constant between the reference and deformed cells instead of applying a k-point density, to prevent abrupt changes from interfering with the necessary fits. All values were calculated clamped, i.e., without ionic relaxation, to obtain finite force in well defined structures.

Gibbs energies for melting temperatures and the phase diagram were calculated using the Calphy package [57]. It employs thermodynamic integration via a switching parameter and reversible scaling to obtain Gibbs or Helmholtz energies in a mostly automated manner. Structures were replicated to sizes >10000 atoms and temperature sweep calculations were carried out over 300000 switching steps.

To compute the concentration-temperature phase diagram for our potential, the Gibbs energies G of pure and intermetallic phases in solid and liquid states were calculated using Calphy. The free energies of mixtures were calculated on a concentration-temperature grid in steps of 1 % and 1 K, where the concentration grid was supplemented with the concentrations of intermetallic phases. For solid-solid and solid-liquid mixtures, G was obtained as a linear combination according to the lever rule. G_{liquid} was interpolated to arbitrary concentrations using the Scipy Clough-Tocher 2D interpolator [58]. Phases were treated as stoichometric compounds, i.e., solubility was neglected in all cases. After obtaining G for all possible phases and phase combinations on the concentration-temperature grid, the stable phase was determined at each grid point.

For visualization and analysis of structural features, Ovito Pro [59] was used. The total structure factors (TSFs) were determined on samples containing 256 000 atoms that were quenched from the melt with a rate of 1×10^{11} K/s. For the calculation the radial distribution function was obtained as average of 40 snapshots taken over 1 ns in an NPT simulation at 300 K and 0 Pa.

On an atomistic level, amorphous alloys can be characterized using Voronoi tessellation. The resulting coordination polyhedra are described by their Voronoi index $\langle n_3, n_4, n_5, n_6, ...\rangle$, which denotes the number of 3, 4, 5, 6,... edged faces of the polyhedron. Voronoi indices were determined using the corresponding Ovito functionality for polydisperse Voronoi tessellation with particle radii of 1.35 for Cu and 1.55 for Zr. This is similar to other works [3,60]. Even though exact radii are rarely provided, the possible impact on conclusions in this paper is marginal, as shown in the Supplemental Material [61].

III. RESULTS

Fitting a general purpose MLIP requires that the training data spans a wide phase space, while it may be beneficial to apply stricter filtering criteria for more specialized potentials. Figure 1 summarizes the energy-volume range spanned by our training data and the overall accuracy of the ACE potential in relation to the DFT reference. Formation energies and volumes span a wide range of 10 eV/atom and 150 Å^3/atom over the whole compositional range, as shown in Fig. 1(a). Figures 1(b) and 1(c) show the error of calculated energies as a function of the distance from the convex hull and force correlation for the potential, compared to DFT data. The energy and force root mean square errors (RMSEs) are 11.5 meV/atom and 14.2 meV/atom and 168 meV/Å and 188 meV/Å for the train and testing data sets, respectively. With respect to energy RMSEs of $\sim$1 meV/atom promised by the MLIPs for specific systems [42,62], these numbers seem large. However, higher accuracies are often achieved for single element systems or by applying much stricter filtering criteria to the training and test data. This decreases the error and could help fit potentials for special purposes, but reduces the transferability to different problem settings, opposing the goal of this paper to fit a general purpose potential. Furthermore, as a result of the energy-based weighting scheme, the errors are lower for structures closer to the convex hull, i.e., structures that are important for most problems. This can be seen in Fig. 1(d), which shows the cumulative energy RMSE as a function of the distance from the convex hull, highlighting that a direct comparison to reference energies and forces alone is not a very useful measure to assess the accuracy of MLIPs.

A. Crystalline phases

An accurate description of energies and forces is a necessity for a good potential, but does not directly relate to properties that can be compared to other potentials or experiments. Therefore, some relevant properties of crystalline Cu-Zr phases are evaluated in this section, starting with pure Cu and Zr, before intermetallics are assessed. Table I shows lattice constants, vacancy formation energies, bulk moduli, elastic constants, and transition temperatures of Cu, Zr, and CuZr-B2 calculated with DFT and our ACE potential, as well as experimental data when available.

1. Copper

Cu is a metal with FCC structure and no other polymorphs up to the melting point. As described in the training data section, we also included other structure types in the fit for teaching the potential about unfavorable configurations. In the following, we restrict the discussion to the relevant FCC structure. All results are summarized in Table I.

The Cu-Zr ACE potential shows excellent agreement with the reference DFT data, but slightly overestimates its lattice constant compared to experiments.

Clamped and relaxed vacancy formation energies E^f_{vac} for Cu are lower than the reference DFT values by roughly 0.15 eV, while experimental values for Cu are about 0.2 eV larger. According to Glensk *et al.* [76], the experimental values should be revised, however, because the applied extrapolation from high-temperature measurements to formation energies at 0 K is not taking all anharmonic effects into account. By applying their corrections, a vacancy formation energy of 1.06 eV is obtained for FCC Cu, which fits very well to the results from DFT.

Since the error of E^f_{vac} seems rather large, we used it as a test case and compared the performance of our general purpose Cu-Zr potential to a potential fitted with exactly the same settings, but only to the Cu training data. The resulting potential leads to clamped and relaxed formation energies of $E^{f,\text{clamped}}_{\text{vac}} = 1.12$ eV and $E^f_{\text{vac}} = 1.09$ eV with a much lower error of 0.01 eV. This clearly shows that the use of a limited

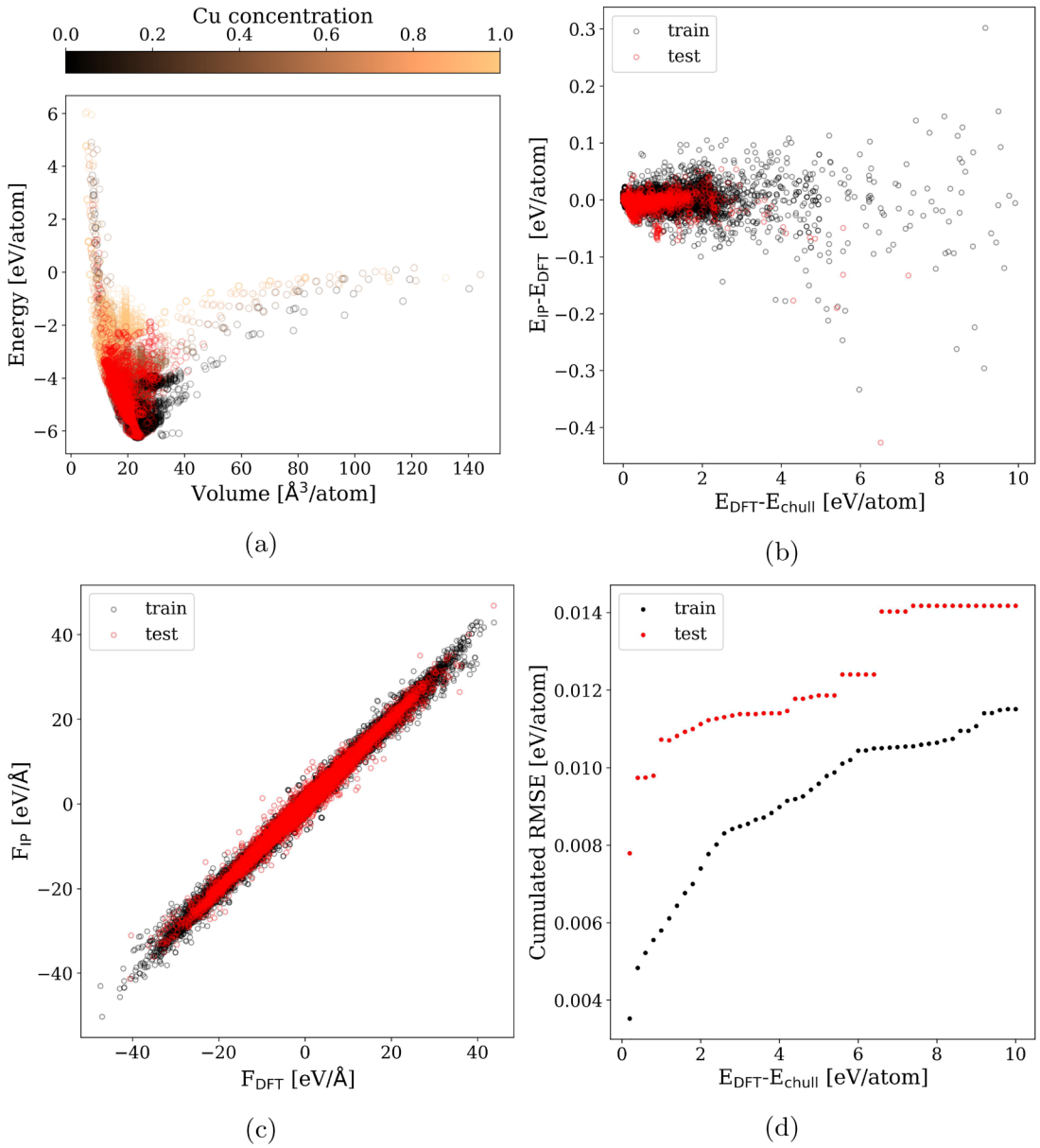

FIG. 1. Energy-volume relation of the training and test data sets (a), energy error with respect to the distance from the convex hull (b), force scatter plot (c), and cumulative energy RMSE as function of the distance from the convex hull (d). In (b) and (d), the impact of using training data that covers a wide range of energies and of the applied energy based weighting scheme can be observed.

training data set can be beneficial when fitting a potential for a specific purpose.

Bulk modulus and other elastic constants are well described, both in comparison with DFT and with experimental data. The melting temperatures calculated with the MB method and CALPHY agree well, but are about 135 K lower than the experimental value. An underestimation of melting points is expected when using the PBE functional and indeed the ACE value corresponds well to the one reported by Zhu *et al.* [73], who developed the TOR-TILD approach to calculate the melting temperature directly from *ab initio* MD simulations.

Another interesting property of FCC metals are the stacking faults occurring on {111} planes. They play an important role for the formation of partial dislocations, twin boundaries and cross slip. Borovikov *et al.* [77] demonstrated that it is possible to fit potentials reproducing several other properties with high accuracy but widely different stacking fault energies, highlighting the importance of explicitly testing this property. For this purpose, we calculated the generalized stacking fault (GSF) energy along the ⟨112⟩ direction and the energy of the gamma surface on a regular 11×11 grid with DFT and our potential. Atoms in the structure were allowed to relax in the direction of the surface normal, but not in plane. The results are shown in Fig. 2. Stable and unstable GSF energies are listed in Table I, again showing good agreement between DFT and potential data with errors of $10\,\mathrm{mJ/m^2}$ and $4\,\mathrm{mJ/m^2}$, respectively.

TABLE I. Lattice constants, bulk moduli, vacancy formation energies, melting temperatures and Cu GSF.

Lattice constants [Å]	Exp.	DFT (0 K)	ACE (0 K)		
Cu_{FCC}	3.602 (0 K) [63]	3.634	3.634		
Zr_{HCP}-a	3.229 (4.2 K) [64]	3.235	3.228		
Zr_{HCP}-c	5.141 (4.2 K) [64]	5.172	5.189		
Z_{BCC}	3.579 (0 K) [65]	3.574	3.576		
CuZr	3.246 (0 K) [66]	3.273	3.272		
E^f_{vac} [eV]	Exp.	Clamped		Relaxed	
		DFT	ACE	DFT	ACE
Cu_{FCC}	1.27-1.29 [67,68]	1.11	0.96	1.08	0.92
Zr_{HCP}	>1.5 [69]	2.06	1.92	1.94	1.88
Zr_{BCC}		2.18	1.82	−0.79	−0.97
B [Gpa]	Exp.	DFT	ACE		
Cu_{FCC}	142 [70]	139	149		
Zr_{HCP}	95 [71]	98	115		
Zr_{BCC}		90	116		
CuZr		121	134		
C_{11}	Exp.	DFT	ACE		
Cu_{FCC}	177 [70]	180	202		
Zr_{HCP}	155 [72]	173	206		
Zr_{BCC}		71	101		
CuZr		143	168		
C_{12}	Exp.	DFT	ACE		
Cu_{FCC}	125 [70]	117	121		
Zr_{HCP}	67 [72]	42	81		
Zr_{BCC}		97	136		
CuZr		110	127		
C_{44}	Exp.	DFT	ACE		
Cu_{FCC}	81 [70]	85	95		
Zr_{HCP}	36 [72]	31	45		
Zr_{BCC}		24	7		
CuZr		44	45		
$T_{transition}$ [K]	Exp.	DFT	ACE (MB)	ACE (Calphy)	
$Cu_{FCC\leftrightarrow Melt}$	1358 [8]	1251 ± 15 [73]	1225	1223	
$Zr_{HCP\leftrightarrow BCC}$	1136 [8]			938	
$Zr_{BCC\leftrightarrow Melt}$	2128 [74]		1693	1699	
$CuZr_{B2\leftrightarrow Melt}$	1208–1233 [8,9,75]		870 ± 50	865	
Cu GSF energy [mJ/m^2]	DFT	ACE			
Stable	41	31			
Unstable	171	167			

2. Zirconium

Zr is more complex than Cu. At room temperature, it has a HCP structure and undergoes a phase transition to BCC before melting.

The lattice constants for both phases deviate by less than 1% from the experimental and DFT data. Both transition temperatures are underestimated compared to experiment, as expected for PBE, but in this case no DFT data is available for direct comparison. Experimentally, the Zr vacancy formation energy is not measured with high accuracy, but DFT and ACE values agree reasonably well. For BCC Zr, the relaxed vacancy formation energy at 0 K is negative. This happens because the structure has a soft phonon that collapses to one where many atoms have HCP-like coordination during relaxation, which is energetically favorable at 0 K. Elastic constants are not described as well as in the case of Cu. Again, this could be improved by fitting a specialized Zr potential, but we assume that the more complex nature of Zr-Zr bonds with stronger angular dependencies leads to lower accuracies for the same set of basis functions. For testing this assumption, we also fitted a potential with the same settings to the Zr training data, only, and obtained an RMSE for the energies of 14.7 meV/atom compared to 3.1 meV/atom for the pure Cu potential. Since training data sets for Cu and Zr were produced and filtered with the same procedure, the much larger error

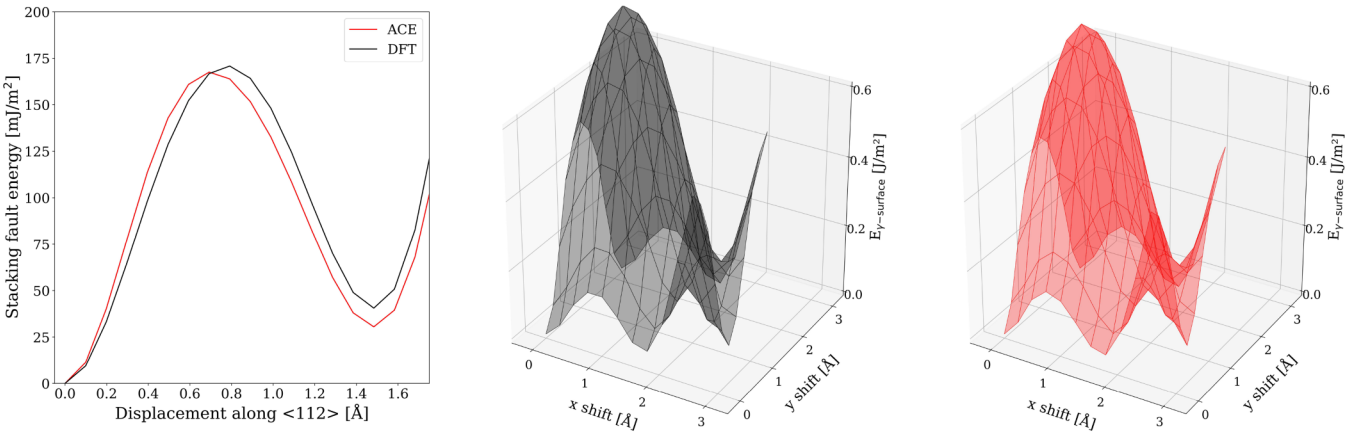

(a) GSF energy (b) γ surface DFT (c) γ surface ACE

FIG. 2. Cu GSF energy along ⟨112⟩ on a {111} plane and γ surface calculated with DFT and ACE.

for Zr is indicative for the higher complexity of interatomic interaction in this metal.

3. *Intermetallic phases*

Cu-Zr alloys can form several intermetallic phases. Their exact composition, crystal structure, and stability range are controversially discussed and, therefore, published phase diagrams differ significantly [11,12].

The phase diagram calculated with our potential is shown in Fig. 3 in comparison to the result of He *et al.* [10], which was chosen as reference because it is consistent with the PBE training data except for the low temperature stability of Cu_5Zr. For the calculated phase diagram, the 0 K formation energies were shifted to the DFT values, which is necessary to stabilize the Cu_8Zr_3 phase. A version without the corrections is provided in the Supplemental Material Fig. S5 [61]. Besides the wrong melting points, that are expected when using PBE data, good agreement with the experimental work is achieved, especially for the Cu rich side. In the following, we will shortly discuss each Cu-Zr phase present in the phase diagram starting at low Zr concentrations.

The intermetallic phase Cu_5Zr is missing in our computed phase diagram. Its Gibbs energy compared to the stable phases is shown in Fig. 3(d). An energetic shift of a few meV/atom would stabilize it. This instability can be directly attributed to the PBE reference data, which places it about 8 meV/atom above the convex hull. Other authors included a Cu_9Zr_2 phase instead of the Cu_5Zr one [8,9,78], and sometimes the phase is considered stable only at elevated temperatures [12].

For $Cu_{51}Zr_{14}$, the calculated melting point agrees very well with the data of He *et al.* Sometimes this phase is considered the high-temperature phase [78,79].

Similar to $Cu_{51}Zr_{14}$ the phase transition temperature of Cu_8Zr_3 is well reproduced. Again some authors suggest that it is only stable at elevated temperatures [7,9,78,79].

$Cu_{24}Zr_{13}$ and/or Cu_2Zr are sometimes included in phase diagrams [7,9,12,78] over very small stability ranges at elevated temperatures, but their crystal structure and exact composition remain unclear and other authors considered them artifacts of the applied experimental procedure [8,80].

For $Cu_{10}Zr_7$ some authors again suggested an eutectoidal decomposition at lower temperatures [12,81], while it lies on the convex hull according to our DFT data.

CuZr-B2 should become thermodynamically stable at elevated temperatures, but this phase does not appear in the calculated phase diagram. Figure 3(d) shows its Gibbs energy compared to the stable $Cu_{10}Zr_7$-Cu_2Zr mixture. A very small difference of 5 meV/atom would be sufficient to change the transition temperature from roughly 1350 K predicted by our potential to the experimental value. Technologically, this phase is of interest because it undergoes a martensitic phase transition from the B2 to B33 and B19' structures upon fast quenching or mechanical deformation. This phase transformation was found to improve the ductility when included in glass samples [82] (see also Sec. III C) and causes a shape memory effect [83]. Therefore, we investigated the dynamic stability of B2 and the phase transition in more detail. In the harmonic approximation, the potential predicts B2, B19', and B33 CuZr to be dynamically unstable at 0 K, as they show soft phonon modes (phonon dispersions calculated with PHONOPY [84,85] are shown in the Supplemental Material [61]). However, MD simulations of small B2 and B19' particles did not show a spontaneous phase change. To further investigate this, we calculated the finite temperature phonon dispersion containing anharmonic effects up to fourth order of the B2 phase, which is shown in Fig. 4(a). It does not contain any soft modes. The calculations were done with the self-consistent phonon method implemented in ALAMODE [86,87].

According to the work of Hatcher *et al.* [88,89], the B2-B19' transition does not have a barrier for the common shape memory alloy NiTi in DFT calculations when following a specific two-step transformation path. First, the middle two layers of a six-layer {011} B2 structure are displaced by half $a_0/2$ along the ⟨100⟩ direction. Then the monoclinic angle changes to the equilibrium one. Following this path for B2 CuZr, we found a small barrier for the first step and no barrier for the second. The corresponding energy is shown in Fig. 4(b). Table I includes several properties of the B2 phase compared with DFT data and experiment when available.

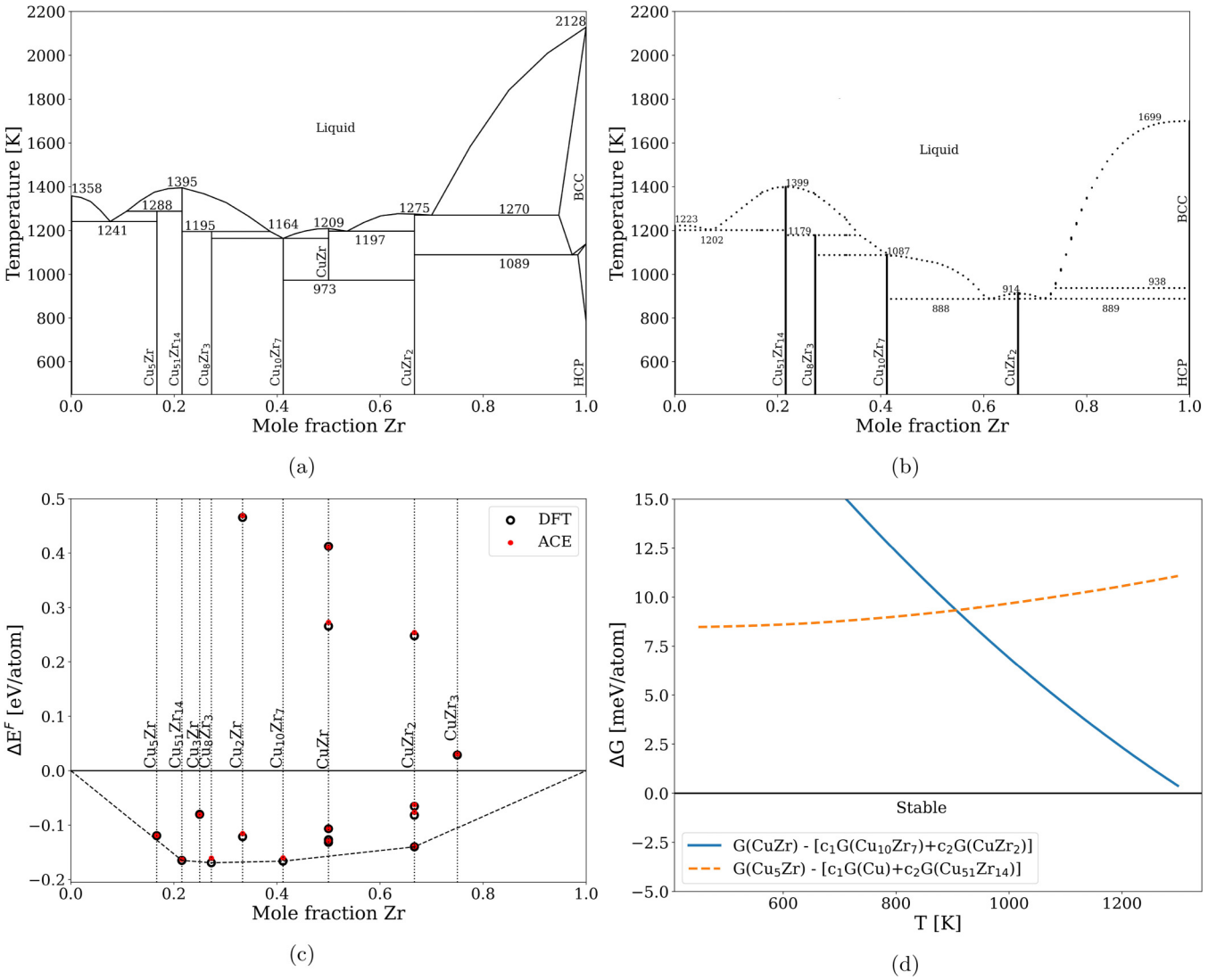

FIG. 3. Phase diagrams based on the work of He *et al.* [10] (a) and calculated with our potential (b), along with 0 K formation energies calculated with DFT and ACE (c), and Gibbs energies of Cu_5Zr and CuZr phases compared to the stable two phase mixtures at corresponding concentrations as calculated with ACE. For (b) and (d), formation energies at 0 K were shifted to the DFT values.

Some phase diagrams include Cu_5Zr_7 or Cu_5Zr_8 [7,9,78,79], which becomes stable in a similar temperature range as CuZr, but again their crystal structure is unclear. Additionally, they did not occur in annealing experiments by Zhou and Napolitano [81].

$CuZr_2$ occurs in all phase diagrams and is stable from 0 K up to the melting point, which is heavily underestimated for our potential. Sometimes a high- and low-temperature modification with $I4/mmm$ and an unresolved superstructure of it are considered, where the transition occurs around 1200 K [7,9]. In our case, we used the $I4/mmm$ structure, which is stable at 0 K according to our DFT data and was used by most authors [8,78,81].

We expect that neglecting solubility causes a small error in the region close to pure Zr, because the HCP and, especially, the BCC phases show a solubility of a few percent, while all other phases are line compounds according to published phase diagrams. The minor energetic differences necessary to stabilize Cu_5Zr and CuZr illustrate the capabilities of modern MLIPs, but also their limits due to the lack of more accurate reference data. Here, the MLIP-aided calculation of phase diagrams could be used in the development of exchange-correlation functionals by offering another way to evaluate them. Another promising route for improvements is the direct use of experimental data for the fitting process, which has seen considerable progress and was recently implemented for some neural network based potentials [90–92].

Errors in formation energies compared to DFT data for our potential and classical IPs from Mendelev *et al.* (EAM), Kim and Lee (Modified Embedded Atom Method (MEAM)), and Păduraru *et al.* (Effective Medium Theory (EMT)) [27,29,31,93] are shown in Fig. 5. As can be seen, the formation energy is accurately reproduced for all structures included in the training data, while classical potentials have much higher errors. DFT data calculated using the Perdew-Wang exchange-correlation functional was used for the Mendelev

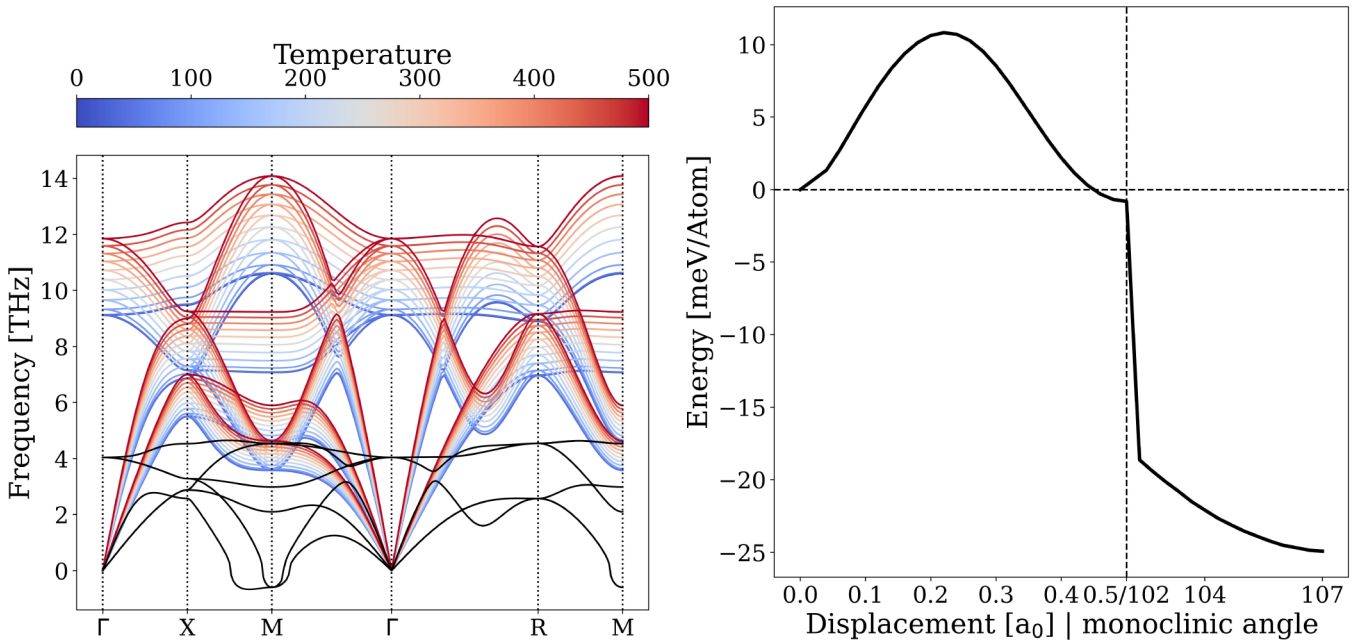

FIG. 4. Finite-temperature phonon dispersion including anharmonic interactions calculated with the self-consistent phonon method (a). For comparison, the phonon dispersion as calculated with the harmonic approximation is shown as a black line. Also shown is the energy along the transformation path from B2 to B19' used by Hatcher *et al.* [88] for NiTi (b). Contrary to their findings for NiTi, our potential predicts a small barrier for CuZr.

and Paduraru potentials, so the results should be comparable. The Kim potential was fitted to experimental data for CuZr.

The extrapolation behavior is tested with the C14, C15, and C36 Laves phases, which were not included in the training data. We have chosen Laves phases because systems with similar ionic radii and some ternary compounds including Cu-Zr have stable C14 or C15 phases [94,95]. Additionally, the C14 phase is stable at room temperature for the Mendelev Cu-Zr potential from 2009 [96] and energetically very favorable compared to the amorphous phase. In combination with a low kinetic barrier, this leads to crystal nucleation on timescales accessible via MD simulations [97], thus showing the importance of an accurate description of formation enthalpies.

For the Laves phases, the ACE potential performs worse compared to the structures explicitly included in the training data, but even when extrapolating it performs much better than the classical potentials. Note that the Mendelev potential used for the comparison is the version from 2019 [31], which

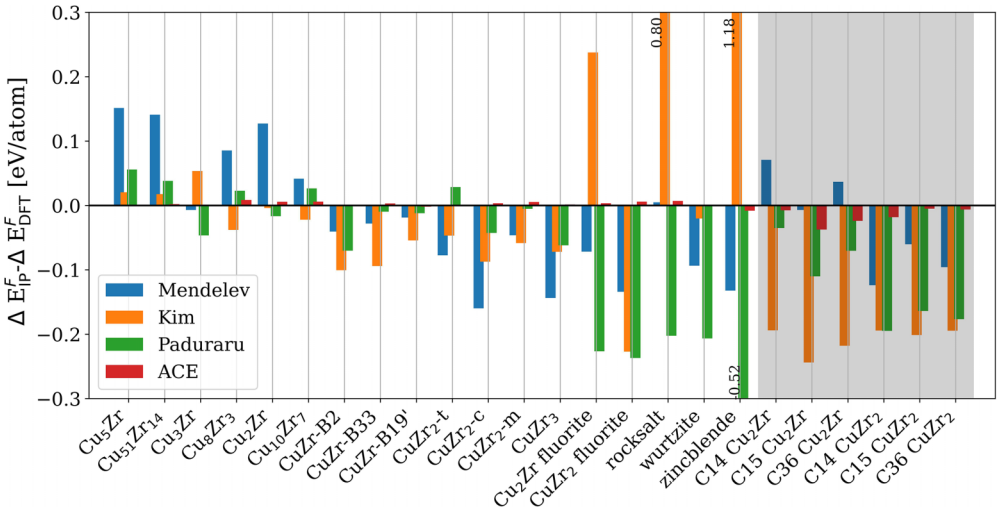

FIG. 5. Errors in formation energy of our ACE and several classical IPs compared to DFT data for structures included in training (white background) and extrapolating to Laves phases (gray shaded area). All formation energies are calculated with respect to Cu_{FCC} and Zr_{HCP}.

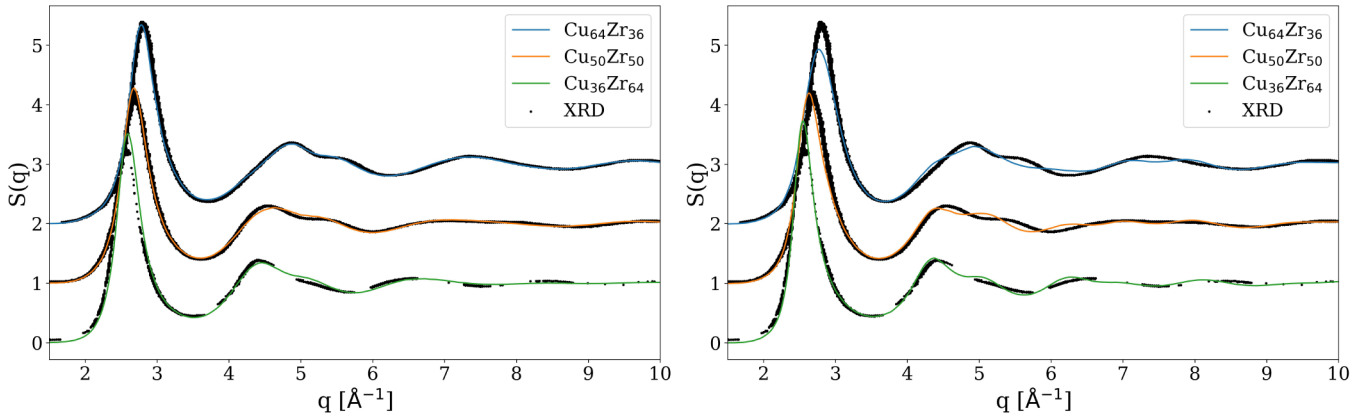

(a) ACE MLIP (b) Mendelev EAM

FIG. 6. Total structure factor of MGss at 300 K simulated with the ACE MLIP (a) and Mendelev EAM potential (b) in comparison to XRD data from Ref. [98]. Experimental compositions were $Cu_{65}Zr_{35}$ and $Cu_{35}Zr_{65}$ instead of $Cu_{64}Zr_{36}$ and $Cu_{36}Zr_{64}$, respectively. S(q) are shifted by +2 and +1 for $Cu_{64}Zr_{36}$ and $Cu_{50}Zr_{50}$ to make them more visible. The data obtained with the Mendelev potential do not show an accurate splitting of the second peak. Additionally, the height of the first peak of $Cu_{64}Zr_{36}$ is much more accurate for the ACE potential.

reduced the overstabilization by including the formation energy of Cu_2Zr Laves phases in the fit and consequently manages to outperform our ACE for C15 Cu_2Zr.

B. Amorphous structure

The structure of Cu-Zr MGss has been the topic of several experimental and theoretical studies [3,32,98,99]. However, on the atomistic scale, many details are still unclear and results are contradictory. Here, we will discuss details of the amorphous structure produced by our ACE potential and show that common assumptions established due to the usage of empirical potentials are inconsistent with DFT and experimental data.

1. Comparison with experiment

To be able to compare structures produced with our potential with experimental data, we calculated their TSF, which can also be obtained directly by diffraction experiments. In Fig. 6(a), the TSF of 256 000 atom samples quenched from the melt with a quench rate of 1×10^{11} K/s using ACE is shown together with x-ray diffraction measurements from Mattern *et al.* [98]. For comparison, Fig. 6(b) shows the TSF for structures produced in the same manner, but using the Mendelev potential, which was chosen due to its capability to excellently describe the TSF of the melt [31]. The ACE data matches very well with the X-ray diffraction (XRD) data, indicating excellent reproduction of experimental structures. The Mendelev structures, on the other hand, do not show accurate splitting of the second peak. Additionally, the height of the first peak of $Cu_{64}Zr_{36}$ is much more accurate for the ACE potential.

2. Topology

The TSF obtained for the structures quenched with the ACE MLIP agrees excellently with data directly accessible by experiments. Now we focus on local structural motifs characterized by Voronoi polyhedra. In the existing literature on Cu-Zr using MD simulations, Cu-centered full icosahedras (FIs) with the Voronoi index $\langle 0, 0, 12, 0\rangle$ are considered to be the primary structural motif in amorphous Cu-Zr [3,97,100,101]. For example, Ding *et al.* [3] found up to 25.6 %, respectively, 22.4 % of all atoms being in the center of a FI for the Cheng [32] and Mendelev (2009) potentials [30] in $Cu_{64}Zr_{36}$ MGss [102].

Direct experimental quantification of Voronoi polyhedra is not possible. Single diffraction measurements can measure the TSF. Partial pair correlation functions can be obtained by combining multiple diffraction experiments, but they do not give an atomistic picture of the structure. Thus, a combination with atomistic models is required to obtain more insights. Mattern *et al.* studied Cu-Zr MGss using a combination of diffraction experiments and reverse Monte Carlo modeling and found FIs in much smaller fractions of 6.3% of all atoms for $Cu_{65}Zr_{35}$ [98]. They report a plethora of different structural motifs instead of a single dominating one. The reason for this could be, however, that Reverse Monte-Carlo (RMC) always finds the most random structure that fulfills a certain convergence criterion [3].

Figure 7 shows the population of structural motifs in the glass samples also used to calculate the TSF. All motifs that occurred with a frequency of at least 1% in one of the compositions are included. Similar to the structure proposed by Mattern *et al.,* no dominating motif exists. Additionally, the amount of FIs corresponds very well to their reported values of 6.3%, 4.5% and 3.5% for $Cu_{65}Zr_{35}$, $Cu_{50}Zr_{50}$, and $Cu_{35}Zr_{65}$ respectively. As previous simulation studies found that the fraction of atoms in the FI motif increased drastically with decreasing quench rates [3,31], we calculated their amount for samples quenched with 1×10^{14} K/s to 1×10^{11} K/s. The result is shown in the Supplemental Material in Fig. S7 [61]. Far less FI were found with respect to the quench rate than, for example, in Refs. [31,101]. Furthermore, their number increased only slightly with decreasing quench rates. Considering these results and the excellent agreement with the experimental TSF, we do not expect major changes in the structures when using lower quench rates.

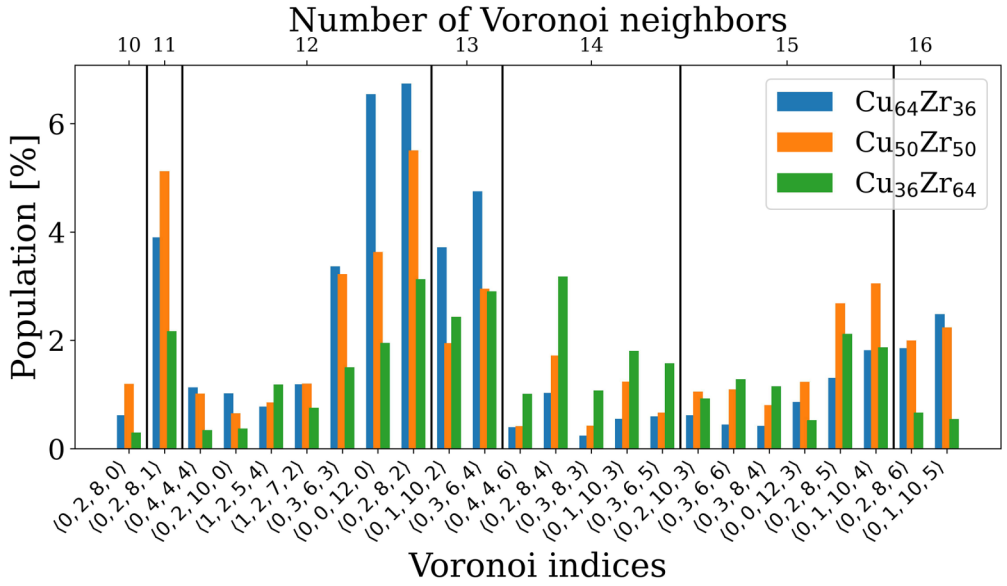

FIG. 7. Population of Voronoi polyhedra in ACE MGs samples.

3. Energetics

Finally, we investigated how the structure influences the energetics of the amorphous phase. Therefore, we compared MGs structures produced with ACE and the Mendelev 2019 potential. For each potential and composition, three samples with 256 atoms were produced using a quench rate of 1×10^{10} K/s. Then, volume and atomic positions were relaxed with DFT, and both potentials and their formation energies were calculated. The results are shown in Fig. 8. As can be seen, DFT and ACE values agree very well across all samples and the structures produced with ACE are favorable according to both DFT and ACE data, while the Mendelev potential predicts its own structures to be more stable. The DFT data suggests that MGss with higher Cu concentrations have lower formation energies, compared to their Zr rich counterparts. The Mendelev potential, however, predicts the Zr rich glasses to be more stable.

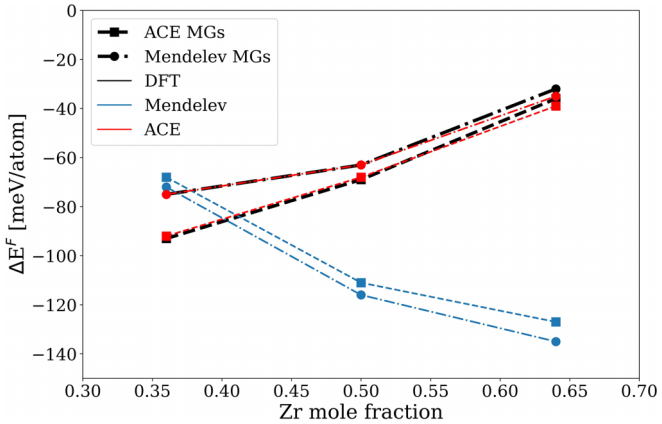

FIG. 8. Formation energy of MGs samples produced with ACE and Mendelev potentials as calculated with DFT, ACE, and Mendelev potentials. Cu_{FCC} and Zr_{HCP} were used as reference states.

DFT relaxation also gave an additional hint that the amount of FIs coordinated atoms is heavily overestimated by previous potentials. An analysis of the structural motifs of the Mendelev samples before and after relaxation with DFT showed that out of the 768 atoms for each composition, the number of FI coordinated ones reduced from 112 to 108, 41 to 34, and 17 to 14 for $Cu_{64}Zr_{36}$, $Cu_{50}Zr_{50}$, and $Cu_{36}Zr_{64}$, respectively.

C. Tensile tests

Previous studies found that the FI motif leads to an increased shear localization and generally has a large impact on the deformation behavior of MGss [97,101,103,104]. Ding *et al.* even found a massive change in the shear modulus of Cu-Zr glasses, once enough FIs were present for percolation [3]. Since we found far less of the perfect $\langle 0, 0, 12, 0\rangle$ polyhedra, we tested the behavior of glass samples with varying compositions under mechanical load. Figure 9 shows $Cu_{36}Zr_{64}$, $Cu_{50}Zr_{50}$, and $Cu_{64}Zr_{36}$ under tensile strain at 50 and 300 K. At 50 K, shear bands form for all compositions, leading to strain localization. A more homogeneous formation of shear transition zones can be observed at 300 K. These results agree well with previous works [105], despite the massively different glass structures observed for the new potential. The simulations were carried out with a strain rate of 4×10^{7} 1/s and periodic boundary conditions in all dimensions. Tensile samples were generated by a $6\times2\times6$ replication of smaller cubic samples containing 10 976 atoms that were quenched with 5×10^{10} K/s. The final structures were annealed at 450 K for 0.5 ns to reduce the artificial periodicity and create a more realistic glass.

The observed formation of shear bands leads to the brittle failure of MGss. Their plasticity can be improved by the inclusion of crystalline precipitates [20–22] due to the interaction of shear bands with the reinforcing phase. Furthermore, the

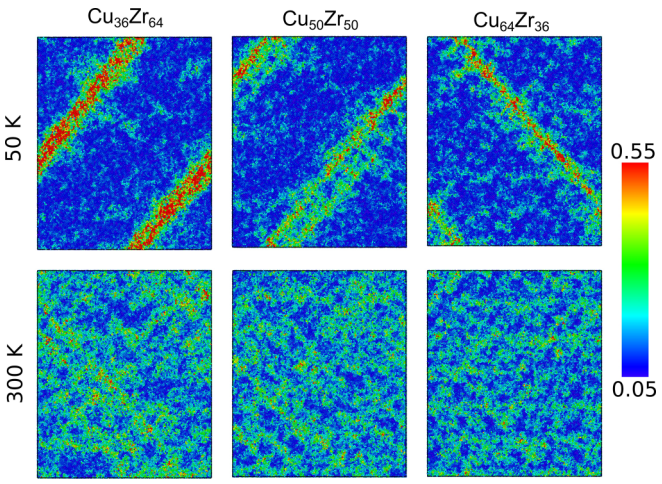

FIG. 9. Atomic strain in tensile tests of Cu-Zr glasses with different compositions and at different temperatures. Snapshots were taken at 12% strain. At low temperatures, the strain is localized in shear bands. At high temperatures, multiple shear transition zones are activated, leading to a more homogeneous deformation mechanism.

martensitic B2 to B19' phase transition of CuZr precipitates in glasses was found to lead to work hardening in experiments [82,106,107]. To understand the role of the martensitic phase transition on an atomistic level, we performed tensile tests on a $Cu_{50}Zr_{50}$ glass matrix with a spherical CuZr inclusion. The sample was produced by replicating the previous $Cu_{50}Zr_{50}$ sample by $1\times2\times1$ to a size of $34.5\times23\times34.5$ nm. A spherical CuZr-B2 crystal with a diameter of 14 nm was included. It was annealed for 0.5 ns at 450 K to obtain a more realistic glass-crystal interface. Figure 10 shows snapshots of the atomic strain and crystal structure during loading. First, the interface between the phases serves as a nucleation site for shear transition zones at the top and bottom of the inclusion. Then a shear band starts to form in the amorphous matrix, while the martensitic phase transition starts to take place in the crystal. Both occur at a 45ºÂ° angle to the loading direction, i.e., in the direction with the highest shear stress. Finally, a mature shear band is formed and an area of similar width in the crystal is transformed to the B19' phase. These findings agree well with *in situ* neutron diffraction experiments from Wu *et al.* [108], who found that the phase transition occurs together with macroscopic yielding, corresponding to the formation of shear bands in the simulations.

Structures were identified by comparing them to the reference structures using the Smooth Overlap of Atomic Positions (SOAP) descriptor [40] as implemented in DSCRIBE [109]. The similarity between two structures was measured as

$$\left(\frac{\vec{S}_1\cdot\vec{S}_2}{\sqrt{|\vec{S}_1|\cdot|\vec{S}_2|}}\right)^4, \tag{3}$$

where $\vec{S}_1$ and $\vec{S}_2$ are the soap vectors of the two structures to compare.

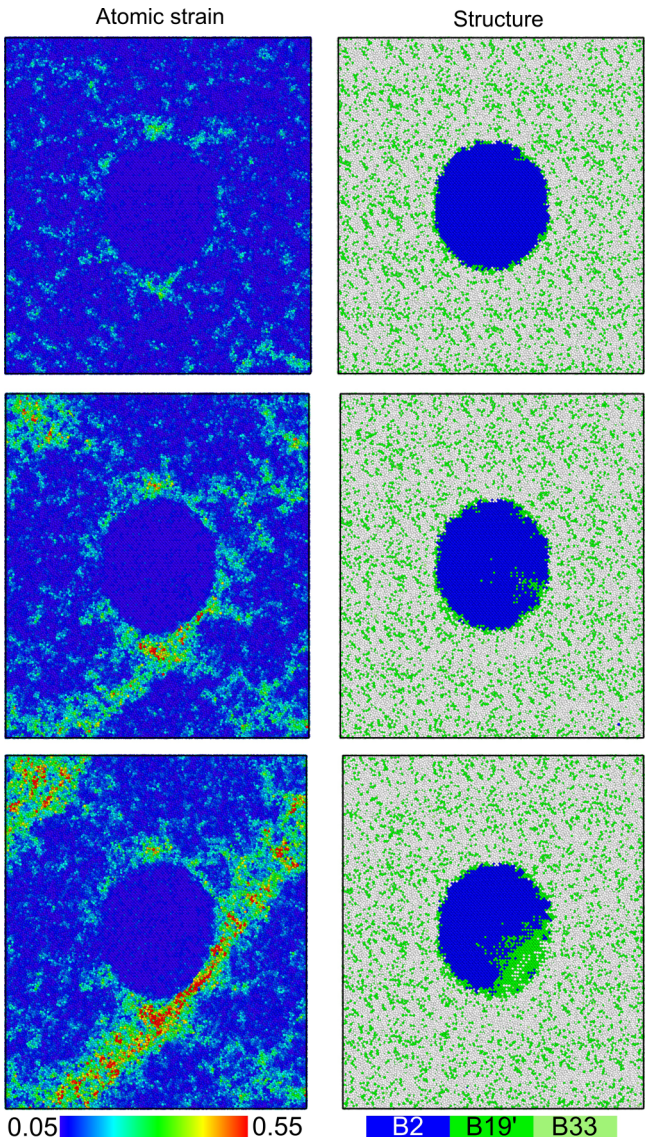

FIG. 10. Shear band formation and structure evolution of a $Cu_{50}Zr_{50}$ matrix with a crystalline CuZr-B2 inclusion. The strain localizes at the interface until a shear band is formed. A martensitic phase transition from the B2 to B19' structure of roughly the same width as the shear band can be observed in the crystalline phase.

IV. CONCLUSION

An ACE MLIP for the MGs forming Cu-Zr system was fitted. It is capable of reproducing DFT reference data with high accuracy, while being applicable to simulations with millions of atoms.

Using the ML potential in conjunction with CALPHY, a temperature-composition phase diagram was calculated. It shows good agreement with experimentally determined phase diagrams within the accuracy limits defined by the usage of PBE reference data. The description of formation energies of intermetallic compounds is much better than with other available potentials.

Amorphous structures produced with cook and quench simulations show very good agreement with experimental XRD data and a detailed Voronoi analysis revealed far fewer FI units than predicted by embedded atom-type classical potentials. Instead, a plethora of different structural motifs exists in the glass. The results are in agreement with RMC models and DFT tests conducted on small MGs samples.

Despite the structural differences, tensile tests on MGs samples showed qualitative agreement with previous results, with shear bands only forming at very low temperatures for the quench rates achievable in MD simulations. The inclusion of a B2-CuZr sphere in a $Cu_{50}Zr_{50}$ glass matrix showed that the crystal undergoes a martensitic phase transition to the B19' phase upon interaction with a shear band.

In summary, this ACE potential for Cu-Zr allows gaining unique insights into structure-property relations of MGss, since it provides DFT accuracy and reproduces various experimental results better than classical IPs.

The potential files, input used for fitting, as well as training and test data are freely accessible on zenodo under [52].

ACKNOWLEDGMENTS

N.L. acknowledges L. C. Erhard for helpful discussions. This research was funded by the Deutsche Forschungsgemeinschaft (DFG, German Research Foundation) under Grant No. 405621137. We gratefully acknowledge computing time provided by the high performance computer Lichtenberg at the NHR Center NHR4CES at TU Darmstadt. K.A. acknowledges support from the DFG under Grant No. 405621160.

[1] M. I. Mendelev, D. J. Sordelet, and M. J. Kramer, Using atomistic computer simulations to analyze x-ray diffraction data from metallic glasses, J. Appl. Phys. **102**, 043501 (2007).

[2] Y. Ritter and K. Albe, Chemical and topological order in shear bands of $Cu_{64}Zr_{36}$ and $Cu_{36}Zr_{64}$ glasses, J. Appl. Phys. **111**, 103527 (2012).

[3] J. Ding, Y.-Q. Cheng, and E. Ma, Full icosahedra dominate local order in $Cu_{64}Zr_{34}$ metallic glass and supercooled liquid, Acta Mater. **69**, 343 (2014).

[4] T. Brink, M. Peterlechner, H. Rösner, K. Albe, and G. Wilde, Influence of crystalline nanoprecipitates on shear-band propagation in Cu-Zr-Based metallic glasses, Phys. Rev. Appl. **5**, 054005 (2016).

[5] C. X. Peng, D. Şopu, Y. Cheng, K. K. Song, S. H. Wang, J. Eckert, and L. Wang, Deformation behavior of designed dual-phase CuZr metallic glasses, Mater. Des. **168**, 107662 (2019).

[6] A. A. Deshmukh, J. G. Bhatt, P. M. Gade, and S. Pal, Investigation of structural evolution in the Cu–Zr metallic glass at cryogenic temperatures by using molecular dynamics simulations, J. Mol. Model. **27**, 286 (2021).

[7] E. Kneller, Y. Khan, and U. Gorres, The alloy system copper-zirconium, Z. Metallkd. **77**, 43 (1986).

[8] D. Arias and J. P. Abriata, Cu-Zr (Copper-Zirconium), J. Phase Equilib. **11**, 452 (1990).

[9] N. Wang, C. Li, Z. Du, F. Wang, and W. Zhang, The thermodynamic re-assessment of the Cu–Zr system, Calphad **30**, 461 (2006).

[10] X. C. He, H. Wang, H. S. Liu, and Z. P. Jin, Thermodynamic description of the Cu–Ag–Zr system, Calphad **30**, 367 (2006).

[11] H. Okamoto, Cu-Zr (Copper-Zirconium), J. Phase Equilib. Diffus. **29**, 204 (2008).

[12] H. Okamoto, Cu-Zr (Copper-Zirconium), J. Phase Equilib. Diffus. **33**, 417 (2012).

[13] Y. Calvayrac, J. P. Chevalier, M. Harmelin, A. Quivy, and J. Bigot, On the stability and structure of Cu—Zr based glasses, Philos. Mag. B **48**, 323 (1983).

[14] K. H. J. Buschow, Short-range order and thermal stability in amorphous alloys, J. Phys. F **14**, 593 (1984).

[15] T. Mei-Bo, Z. De-Qian, P. Ming-Xiang, and W. Wei-Hua, Binary Cu–Zr bulk metallic glasses, Chin. Phys. Lett. **21**, 901 (2004).

[16] B. F. Lu, L. T. Kong, K. J. Laws, W. Q. Xu, Z. Jiang, Y. Y. Huang, M. Ferry, J. F. Li, and Y. H. Zhou, EXAFS and molecular dynamics simulation studies of Cu-Zr metallic glass: Short-to-medium range order and glass forming ability, Mater. Charact. **141**, 41 (2018).

[17] A. Inoue, Stabilization of metallic supercooled liquid and bulk amorphous alloys, Acta Mater. **48**, 279 (2000).

[18] J. F. Löffler, Bulk metallic glasses, Intermetallics **11**, 529 (2003).

[19] M. F. Ashby and A. L. Greer, Metallic glasses as structural materials, Scr. Mater. **54**, 321 (2006).

[20] C. C. Hays, C. P. Kim, and W. L. Johnson, Microstructure controlled shear band pattern formation and enhanced plasticity of bulk metallic glasses containing *in situ* formed ductile phase dendrite dispersions, Phys. Rev. Lett. **84**, 2901 (2000).

[21] C. Fan, R. T. Ott, and T. C. Hufnagel, Metallic glass matrix composite with precipitated ductile reinforcement, Appl. Phys. Lett. **81**, 1020 (2002).

[22] J. Eckert, J. Das, S. Pauly, and C. Duhamel, Mechanical properties of bulk metallic glasses and composites, J. Mater. Res. **22**, 285 (2006).

[23] Y. Zhang, C. Z. Wang, M. I. Mendelev, F. Zhang, M. J. Kramer, and K. M. Ho, Diffusion in a Cu-Zr metallic glass studied by microsecond-scale molecular dynamics simulations, Phys. Rev. B **91**, 180201(R) (2015).

[24] D. Şopu and K. Albe, Influence of grain size and composition, topology and excess free volume on the deformation behavior of Cu–Zr nanoglasses, Beilstein J. Nanotechnol. **6**, 537 (2015).

[25] M. Sepúlveda-Macías, N. Amigo, and G. Gutiérrez, Onset of plasticity and its relation to atomic structure in CuZr metallic glass nanowire: A molecular dynamics study, J. Alloys Compd. **655**, 357 (2016).

[26] K. F. Gan, S. S. Jiang, Y. J. Huang, H. B. C. Yin, J. F. Sun, and A. H. W. Ngan, Elucidating how correlated operation of shear transformation zones leads to shear localization and fracture in metallic glasses: Tensile tests on CuZr based metallic-glass

microwires, molecular dynamics simulations, and modelling, Int. J. Plast. **119**, 1 (2019).

[27] A. Păduraru, A. Kenoufi, N. P. Bailey, and J. Schiøtz, An interatomic potential for studying CuZr bulk metallic glasses, Adv. Eng. Mater. **9**, 505 (2007).

[28] K. H. Kang, I. Sa, J. C. Lee, E. Fleury, and B. J. Lee, Atomistic modeling of the Cu–Zr–Ag bulk metallic glass system, Scr. Mater. **61**, 801 (2009).

[29] Y.-M. Kim and B.-J. Lee, A modified embedded-atom method interatomic potential for the Cu–Zr system, J. Mater. Res. **23**, 1095 (2008).

[30] M. I. Mendelev, M. J. Kramer, R. T. Ott, D. J. Sordelet, D. Yagodin, and P. Popel, Development of suitable interatomic potentials for simulation of liquid and amorphous Cu–Zr alloys, Philos. Mag. **89**, 967 (2009).

[31] M. I. Mendelev, Y. Sun, F. Zhang, C. Z. Wang, and K. M. Ho, Development of a semi-empirical potential suitable for molecular dynamics simulation of vitrification in Cu-Zr alloys, J. Chem. Phys. **151**, 214502 (2019).

[32] Y. Q. Cheng, E. Ma, and H. W. Sheng, Atomic level structure in multicomponent bulk metallic glass, Phys. Rev. Lett. **102**, 245501 (2009).

[33] M. S. Daw and M. I. Baskes, Embedded-atom method: Derivation and application to impurities, surfaces, and other defects in metals, Phys. Rev. B **29**, 6443 (1984).

[34] M. W. Finnis and J. E. Sinclair, A simple empirical *N* -body potential for transition metals, Philos. Mag. A **50**, 45 (1984).

[35] K. W. Jacobsen, J. K. Norskov, and M. J. Puska, Interatomic interactions in the effective-medium theory, Phys. Rev. B **35**, 7423 (1987).

[36] M. I. Baskes, Application of the Embedded-Atom method to covalent materials: A semiempirical potential for silicon, Phys. Rev. Lett. **59**, 2666 (1987).

[37] M. I. Baskes, J. S. Nelson, and A. F. Wright, Semiempirical modified embedded-atom potentials for silicon and germanium, Phys. Rev. B **40**, 6085 (1989).

[38] V. L. Deringer, M. A. Caro, and G. Csányi, Machine learning interatomic potentials as emerging tools for materials science, Adv. Mater. **31**, 1902765 (2019).

[39] Y. Mishin, Machine-learning interatomic potentials for materials science, Acta Material. **214**, 116980 (2021).

[40] A. P. Bartók, R. Kondor, and G. Csányi, On representing chemical environments, Phys. Rev. B **87**, 184115 (2013).

[41] A. V. Shapeev, Moment tensor potentials: A class of systematically improvable interatomic potentials, Multiscale Model. Simul. **14**, 1153 (2016).

[42] R. Drautz, Atomic cluster expansion for accurate and transferable interatomic potentials, Phys. Rev. B **99**, 014104 (2019).

[43] A. P. Thompson, H. M. Aktulga, R. Berger, D. S. Bolintineanu, W. M. Brown, P. S. Crozier, P. J. in 't Veld, A. Kohlmeyer, S. G. Moore, T. D. Nguyen, R. Shan, M. J. Stevens, J. Tranchida, C. Trott, and S. J. Plimpton, LAMMPS—a flexible simulation tool for particle-based materials modeling at the atomic, meso, and continuum scales, Comput. Phys. Commun. **271**, 108171 (2022).

[44] Y. Lysogorskiy, C. van der Oord, A. Bochkarev, S. Menon, M. Rinaldi, T. Hammerschmidt, M. Mrovec, A. Thompson, G. Csányi, C. Ortner, and R. Drautz, Performant implementation of the atomic cluster expansion (PACE) and application to copper and silicon, npj Comput. Mater. **7**, 97 (2021).

[45] M. Qamar, M. Mrovec, Y. Lysogorskiy, A. Bochkarev, and R. Drautz, Atomic cluster expansion for quantum-accurate large-scale simulations of carbon, J. Chem. Theory Comput. **19**, 5151 (2023).

[46] I. S. Novikov, K. Gubaev, E. V. Podryabinkin, and A. V. Shapeev, The MLIP package: Moment tensor potentials with MPI and active learning, Mach. Learn.: Sci. Technol. **2**, 025002 (2021).

[47] G. Kresse, J. Furthmüller, and J. Hafner, Theory of the crystal structures of selenium and tellurium: The effect of generalized-gradient corrections to the local-density approximation, Phys. Rev. B **50**, 13181 (1994).

[48] G. Kresse and J. Furthmüller, Efficient iterative schemes for *ab initio* total-energy calculations using a plane-wave basis set, Phys. Rev. B **54**, 11169 (1996).

[49] G. Kresse and J. Furthmüller, Efficiency of *ab-initio* total energy calculations for metals and semiconductors using a plane-wave basis set, Comput. Mater. Sci. **6**, 15 (1996).

[50] J. P. Perdew, K. Burke, and M. Ernzerhof, Generalized gradient approximation made simple, Phys. Rev. Lett. **77**, 3865 (1996).

[51] G. Kresse and D. Joubert, From ultrasoft pseudopotentials to the projector augmented-wave method, Phys. Rev. B **59**, 1758 (1999).

[52] N. Leimeroth, J. Rohrer, and K. Albe, Dataset for "A general purpose potential for glassy and crystalline phases of Cu-Zr alloys based on the ACE formalism" (Version 1), Zenodo (2023), https://doi.org/10.5281/zenodo.8137854.

[53] A. Bochkarev, Y. Lysogorskiy, S. Menon, M. Qamar, M. Mrovec, and R. Drautz, Efficient parametrization of the atomic cluster expansion, Phys. Rev. Mater. **6**, 013804 (2022).

[54] Datacite search, https://janaf.nist.gov/, doi: 10.18434/T42S31 (2013).

[55] J. Janssen, S. Surendralal, Y. Lysogorskiy, M. Todorova, T. Hickel, R. Drautz, and J. Neugebauer, Pyiron: An integrated development environment for computational materials science, Comput. Mater. Sci. **163**, 24 (2019).

[56] S. P. Ong, W. D. Richards, A. Jain, G. Hautier, M. Kocher, S. Cholia, D. Gunter, V. L. Chevrier, K. A. Persson, and G. Ceder, Python Materials Genomics (pymatgen): A robust, open-source Python library for materials analysis, Comput. Mater. Sci. **68**, 314 (2013).

[57] S. Menon, Y. Lysogorskiy, J. Rogal, and R. Drautz, Automated free-energy calculation from atomistic simulations, Phys. Rev. Mater. **5**, 103801 (2021).

[58] P. Virtanen, R. Gommers, T. E. Oliphant, M. Haberland, T. Reddy, D. Cournapeau, E. Burovski, P. Peterson, W. Weckesser, J. Bright, S. J. van der Walt, M. Brett, J. Wilson, K. J. Millman, N. Mayorov, A. R. J. Nelson, E. Jones, R. Kern, E. Larson, C. J. Carey *et al.*, SciPy 1.0: Fundamental algorithms for scientific computing in Python, Nat. Methods **17**, 261 (2020).

[59] A. Stukowski, Visualization and analysis of atomistic simulation data with OVITO—the open visualization tool, Modell. Simul. Mater. Sci. Eng. **18**, 015012 (2010).

[60] X. Z. Gao, M. H. Müser, L. T. Kong, and J. F. Li, Atomic structure and energetics of amorphous–crystalline CuZr interfaces:

A molecular dynamics study, Modell. Simul. Mater. Sci. Eng. **22**, 065007 (2014).

[61] See Supplemental Material at http://link.aps.org/supplemental/10.1103/PhysRevMaterials.8.043602 for additional tests of the potential and employed methods.

[62] J. Behler, Four generations of high-dimensional neural network potentials, Chem. Rev. **121**, 10037 (2021).

[63] A. K. Giri and G. B. Mitra, Extrapolated values of lattice constants of some cubic metals at absolute zero, J. Phys. D **18**, L75 (1985).

[64] J. Goldak, L. T. Lloyd, and C. S. Barrett, Lattice parameters, thermal expansions, and Grüneisen coefficients of zirconium, 4.2 to 1130°K, Phys. Rev. **144**, 478 (1966).

[65] A. Heiming, W. Petry, J. Trampenau, W. Miekeley, and J. Cockcroft, The temperature dependence of the lattice parameters of pure BCC Zr and BCC Zr-2 at.%Co, J. Phys.: Condens. Matter **4**, 727 (1992).

[66] J. Gegner, O. Shuleshova, R. Kobold, D. Holland-Moritz, F. Yang, W. Hornfeck, J. Bednarcik, and D. M. Herlach, *In situ* observation of the phase selection from the undercooled melt in Cu–Zr, J. Alloys Compd. **576**, 232 (2013).

[67] R. R. Bourassa and B. Lengeler, The formation and migration energies of vacancies in quenched copper, J. Phys. F **6**, 1405 (1976).

[68] R. W. Balluffi, Vacancy defect mobilities and binding energies obtained from annealing studies, J. Nucl. Mater. **69-70**, 240 (1978).

[69] G. M. Hood, Diffusion and vacancy properties of α-Zr, J. Nucl. Mater. **139**, 179 (1986).

[70] H. M. Ledbetter, Elastic constants of polycrystalline copper at low temperatures. Relationship to single-crystal elastic constants, Phys. Status Solidi A **66**, 477 (1981).

[71] E. S. Fisher, M. H. Manghnani, and T. J. Sokolowski, Hydrostatic pressure derivatives of the single-crystal elastic moduli of zirconium, J. Appl. Phys. **41**, 2991 (1970).

[72] E. S. Fisher and C. J. Renken, Single-crystal elastic moduli and the hcp $\rightarrow$ bcc transformation in Ti, Zr, and Hf, Phys. Rev. **135**, A482 (1964).

[73] L.-F. Zhu, B. Grabowski, and J. Neugebauer, Efficient approach to compute melting properties fully from *ab initio* with application to Cu, Phys. Rev. B **96**, 224202 (2017).

[74] J. Murray, A. Peruzzi, and J. P. Abriata, The Al-Zr (aluminum-zirconium) system, J. Phase Equilib. **13**, 277 (1992).

[75] M. H. Braga, L. F. Malheiros, F. Castro, and D. Soares, Experimental liquidus points and invariant reactions in the Cu–Zr system, Int. J. Mater. Res. **89**, 541 (1998).

[76] A. Glensk, B. Grabowski, T. Hickel, and J. Neugebauer, Breakdown of the Arrhenius law in describing vacancy formation energies: The importance of local anharmonicity revealed by *ab initio* thermodynamics, Phys. Rev. X **4**, 011018 (2014).

[77] V. Borovikov, M. I. Mendelev, A. H. King, and R. LeSar, Effect of stacking fault energy on mechanism of plastic deformation in nanotwinned FCC metals, Modell. Simul. Mater. Sci. Eng. **23**, 055003 (2015).

[78] W. Gierlotka, K.-C. Zhang, and Y.-P. Chang, Thermodynamic description of the binary Cu–Zr system, J. Alloys Compd. **509**, 8313 (2011).

[79] D. H. Kang and I.-H. Jung, Critical thermodynamic evaluation and optimization of the Ag–Zr, Cu–Zr and Ag–Cu–Zr systems and its applications to amorphous Cu–Zr–Ag alloys, Intermetallics **18**, 815 (2010).

[80] K. J. Zeng, M. Hämäläinen, and H. L. Lukas, A new thermodynamic description of the Cu-Zr system, J. Phase Equilib. **15**, 577 (1994).

[81] S. H. Zhou and R. E. Napolitano, Phase stability for the Cu–Zr system: First-principles, experiments and solution-based modeling, Acta Mater. **58**, 2186 (2010).

[82] S. Pauly, J. Das, J. Bednarcik, N. Mattern, K. B. Kim, D. H. Kim, and J. Eckert, Deformation-induced martensitic transformation in Cu–Zr–(Al,Ti) bulk metallic glass composites, Scr. Mater. **60**, 431 (2009).

[83] Yu. N. Koval, G. S. Firstov, and A. V. Kotko, Martensitic transformation and shape memory effect in ZrCu intermetallic compound, Scr. Metall. Mater. **27**, 1611 (1992).

[84] A. Togo, First-principles phonon calculations with phonopy and phono3py, J. Phys. Soc. Jpn. **92**, 012001 (2023).

[85] A. Togo, L. Chaput, T. Tadano, and I. Tanaka, Implementation strategies in phonopy and phono3py, J. Phys.: Condens. Matter **35**, 353001 (2023).

[86] T. Tadano, Y. Gohda, and S. Tsuneyuki, Anharmonic force constants extracted from first-principles molecular dynamics: Applications to heat transfer simulations, J. Phys.: Condens. Matter **26**, 225402 (2014).

[87] T. Tadano and S. Tsuneyuki, Self-consistent phonon calculations of lattice dynamical properties in cubic $SrTiO_3$ with first-principles anharmonic force constants, Phys. Rev. B **92**, 054301 (2015).

[88] N. Hatcher, O. Yu. Kontsevoi, and A. J. Freeman, Martensitic transformation path of NiTi, Phys. Rev. B **79**, 020202(R) (2009).

[89] N. Hatcher, O. Yu. Kontsevoi, and A. J. Freeman, Role of elastic and shear stabilities in the martensitic transformation path of NiTi, Phys. Rev. B **80**, 144203 (2009).

[90] S. S. Schoenholz and E. D. Cubuk, JAX, M.D. A framework for differentiable physics, J. Stat. Mech. (2021) 124016.

[91] S. Doerr, M. Majewski, A. Pérez, A. Krämer, C. Clementi, F. Noe, T. Giorgino, and G. De Fabritiis, TorchMD: A deep learning framework for molecular simulations, J. Chem. Theory Comput. **17**, 2355 (2021).

[92] S. Thaler and J. Zavadlav, Learning neural network potentials from experimental data via differentiable trajectory reweighting, Nat. Commun. **12**, 6884 (2021).

[93] When the composition is unique, the phases are named by it, but multiple $CuZr_2$ and CuZr structures from the MP have low formation enthalpies. For $CuZr_2$, they are named t, c, and m, corresponding to tetragonal, cubic, and monoclinic structures, while CuZr phases are the high temperature B2 and low temperature B19' and B33 phases. Table S1 lists the names and corresponding MP IDs.

[94] A. Von Keitz and G. Sauthoff, Laves phases for high temperatures—Part II: Stability and mechanical properties, Intermetallics **10**, 497 (2002).

[95] H. Men, S. J. Pang, and T. Zhang, Glass-forming ability and mechanical properties of alloys, Mater. Sci. Eng.: A **408**, 326 (2005).

[96] C. Tang and P. Harrowell, Predicting the solid state phase diagram for glass-forming alloys of copper and zirconium, J. Phys.: Condens. Matter **24**, 245102 (2012).

[97] J. Zemp, M. Celino, B. Schönfeld, and J. F. Löffler, Crystal-like rearrangements of icosahedra in simulated copper-zirconium metallic glasses and their effect on mechanical properties, Phys. Rev. Lett. **115**, 165501 (2015).

[98] N. Mattern, P. Jóvári, I. Kaban, S. Gruner, A. Elsner, V. Kokotin, H. Franz, B. Beuneu, and J. Eckert, Short-range order of Cu–Zr metallic glasses, J. Alloys Compd. **485**, 163 (2009).

[99] T. Fujiwara, H. S. Chen, and Y. Waseda, On the structure and vibrational spectra of Cu-Zr alloy glasses, J. Phys. F **13**, 97 (1983).

[100] Ch. E. Lekka, A. Ibenskas, A. R. Yavari, and G. A. Evangelakis, Tensile deformation accommodation in microscopic metallic glasses via subnanocluster reconstructions, Appl. Phys. Lett. **91**, 214103 (2007).

[101] Y. Q. Cheng, A. J. Cao, H. W. Sheng, and E. Ma, Local order influences initiation of plastic flow in metallic glass: Effects of alloy composition and sample cooling history, Acta Mater. **56**, 5263 (2008).

[102] The original values by Ding *et al.* are 40% and 35% of all Cu atoms. For an easier comparison with the work of Mattern *et al.*, the numbers are given as a fraction of all atoms. To calculate them, we assumed that the fraction of Zr atoms in the center of FI is negligible, so $P_{\mathrm{all}} = P_{\mathrm{Cu}} \cdot c_{\mathrm{Cu}}$, where P denotes the population of FI clusters as fraction of all and only Cu atoms and c the concentration.

[103] A. J. Cao, Y. Q. Cheng, and E. Ma, Structural processes that initiate shear localization in metallic glass, Acta Mater. **57**, 5146 (2009).

[104] L. Zhang, Y.-Q. Cheng, A.-J. Cao, J. Xu, and E. Ma, Bulk metallic glasses with large plasticity: Composition design from the structural perspective, Acta Mater. **57**, 1154 (2009).

[105] K. Albe, Y. Ritter, and D. Şopu, Enhancing the plasticity of metallic glasses: Shear band formation, nanocomposites, and nanoglasses investigated by molecular dynamics simulations, Mech. Mater. **67**, 94 (2013).

[106] Y. Wu, Y. Xiao, G. Chen, C. T. Liu, and Z. Lu, Bulk metallic glass composites with transformation-mediated work-hardening and ductility, Adv. Mater. **22**, 2770 (2010).

[107] D. C. Hofmann, Shape memory bulk metallic glass composites, Science **329**, 1294 (2010).

[108] Y. Wu, D. Ma, Q. K. Li, A. D. Stoica, W. L. Song, H. Wang, X. J. Liu, G. M. Stoica, G. Y. Wang, K. An, X. L. Wang, M. Li, and Z. P. Lu, Transformation-induced plasticity in bulk metallic glass composites evidenced by *in-situ* neutron diffraction, Acta Mater. **124**, 478 (2017).

[109] L. Himanen, M. O. J. Jäger, E. V. Morooka, F. Federici Canova, Y. S. Ranawat, D. Z. Gao, P. Rinke, and A. S. Foster, DScribe: Library of descriptors for machine learning in materials science, Comput. Phys. Commun. **247**, 106949 (2020).